Journal of Quantitative Spectroscopy & Radiative Transfer 178 (2016) 361–378

Contents lists available at ScienceDirect

Journal of Quantitative Spectroscopy & Radiative Transfer

journal homepage: www.elsevier.com/locate/jqsrt

Exact and near backscattering measurements of the linear depolarisation ratio of various ice crystal habits generated in a laboratory cloud chamber

Helen R. Smith [a], [*], Paul J. Connolly [a], Ann R. Webb [a], Anthony J. Baran [b]

[a] The University of Manchester, Oxford Road, Manchester, UK
[b] Met Office, Exeter, UK

A R T I C L E I N F O

Article history:
Received 15 September 2015
Received in revised form
18 January 2016
Accepted 21 January 2016
Available online 2 February 2016

Keywords:
Linear depolarisation ratio
Cirrus
Hollowness
Ray tracing
Back scattering
Ice crystal

A B S T R A C T

Ice clouds were generated in the Manchester Ice Cloud Chamber (MICC), and the backscattering linear depolarisation ratio, δ, was measured for a variety of habits. To create an assortment of particle morphologies, the humidity in the chamber was varied throughout each experiment, resulting in a range of habits from the pristine to the complex. This technique was repeated at three temperatures: $-7\,^{\circ}\mathrm{C}$, $-15\,^{\circ}\mathrm{C}$ and $-30\,^{\circ}\mathrm{C}$, in order to produce both solid and hollow columns, plates, sectored plates and dendrites. A linearly polarised 532 nm continuous wave diode laser was directed through a section of the cloud using a non-polarising 50:50 beam splitter. Measurements of the scattered light were taken at 178°, 179° and 180°, using a Glan–Taylor prism to separate the co- and cross-polarised components. The intensities of these components were measured using two amplified photodetectors and the ratio of the cross- to co-polarised intensities was measured to find the linear depolarisation ratio. In general, it was found that Ray Tracing over-predicts the linear depolarisation ratio. However, by creating more accurate particle models which better represent the internal structure of ice particles, discrepancies between measured and modelled results (based on Ray Tracing) were reduced.

© 2016 The Authors. Published by Elsevier Ltd. This is an open access article under the CC BY license (http://creativecommons.org/licenses/by/4.0/).

1. Introduction

The recent meeting of the Intergovernmental Panel on Climate Change highlighted the role of clouds in the Earth's atmosphere as one of the biggest uncertainties in predicting climate change today [1]. One such cloud type that adds to the uncertainty in predicting climate change is cirrus. This is because the net radiative effect of cirrus can be positive or negative, and the direction and the magnitude of this forcing is highly sensitive to the microphysical properties of the constituent ice particles [2–4]. Such particle properties are typically investigated with the use of Optical Array Probes (OAPs), which use optical arrays to capture 2 dimensional particle images. OAPs include the Stratton Park Engineering Company's Cloud Particle Imager (CPI) [5], the 2 Dimensional Stereo probe (2D-S) [6], the Cloud Imaging Probe (CIP) and the Precipitation Imaging Probe (PIP) by Droplet Measurement Technologies (DMT) [7]. These probes have been used both in situ and in laboratory experiments for the counting, sizing and habit classification of ice particles [8–11]. Although successful in characterising larger particles, the discrete pixel size of the array limits the image resolution, meaning that smaller particles (below 80 μm) cannot be accurately categorised. Small ice crystals in cirrus can be influential on the bulk optical properties of the cloud and therefore the accurate counting and sizing of these smaller particles is crucial [11]. Furthermore, the measurement of other atmospheric

---

[*] Corresponding author.
E-mail address: h.smith20@herts.ac.uk (H.R. Smith).

http://dx.doi.org/10.1016/j.jqsrt.2016.01.030

0022-4073/© 2016 The Authors. Published by Elsevier Ltd. This is an open access article under the CC BY license (http://creativecommons.org/licenses/by/4.0/).

particulates is necessary, not only for determining their optical properties but also due to their role in cloud formation and evolution [12–14]. These small particles cannot be measured using OAPs and therefore other techniques must be employed.

In addition to imaging probes, there currently exists a range of in situ instrumentation, which use singly-scattered light to determine information about the scattering particle. Forward scattering probes, such as the Forward Scattering Spectrometer Probe (FSSP) by Particle Measurement Systems (PMS) [15,16], and the Cloud Droplet Probe (CDP) by DMT [17], measure scattered intensities in a given angular range in the forward direction. These measurements are used to count and size particles based on a Mie approximation for homogeneous spheres. Ice and aerosol particles are generally nonspherical and may also be inhomogeneous, thus limiting the accuracy of forward scattering probes for the sizing of nonspherical particles. The ability to determine particle asphericity is a useful tool, not only for particle sizing but for the determination of thermodynamic phase (by discriminating droplets from small ice). One probe which can differentiate between spherical and nonspherical particles is the Small Ice Detector 3 (SID-3). While this instrument also gathers forward scattered light in the 6–25° range, the optical array is used to capture the 2 dimensional scattering pattern. This pattern can be used not only to size the particle, but also to estimate the particle habit and the surface roughness [18,19]. Near backscattered light is also measured by certain in situ instrumentation such as DMT's CAS-DPOL [20], and Cloud Particle Spectrometer with Polarization Detection (CPSPD) [21] instruments, which measure the linear depolarisation ratio of the scattered light [22,23]. Ice particles depolarise the incident light by internal reflection, effectively rotating the vibration plane of the incident beam. Therefore faceted particles such as ice are more strongly depolarising than water droplets, with measurements of linear depolarisation ratio typically an order of magnitude higher for ice clouds compared with water clouds [24,25]. Measurements from the CAS-DPOL and CPSPD can therefore be used for determining particle asphericity, and in the discrimination of liquid water from ice. Further to in situ instrumentation, ground and space based remote sensing relies on scattered signals to determine particle properties [26–30]. The backscattering linear depolarisation ratio has long been used by LIDAR instruments/analysis to determine the thermodynamic phase, size, orientation and habit of cloud particles.

Each of the instruments discussed so far uses measurements of scattered light to determine microphysical properties based on comparisons to current theoretical or observational data. However, discrepancies between measured and modelled results exist. LIDAR measurements of linear depolarisation ratio in cirrus are typically lower than those predicted by theory [31]. These observations have previously been attributed to preferential crystal orientation and the presence of liquid water [31]. However, interpretations of these data usually rely on simulations from Ray Tracing, where highly idealised particles are assumed [27]. Particle complexities such as inclusions, cavities and surface roughness are known to affect the single scattering properties of ice particles [32–36]. Theoretical studies have shown that indentations on the basal facets (frequently seen in laboratory, in situ and ground based studies in the form of 'hollow' columns) act to significantly reduce the linear depolarisation ratio [37,38]. Similar results were shown during laboratory experiments in the Aerosol Interaction and Dynamics in the Atmosphere (AIDA) chamber where low depolarisation ratios of 0.1–0.15 were recorded using the Scattering Intensity Measurement for the Optical detectioN of icE (SIMONE) instrument for a cloud comprised predominantly of hollow columns [39]. By comparison, a cloud composed of solid crystals was measured to have significantly higher depolarisation ratios of 0.3 [39]. By incorporating these particle cavities (along with further complexities such as inclusions and particle roughness) geometric particle models may be improved, thus yielding more realistic values of linear depolarisation ratio from Ray Tracing simulations.

From the current literature, we see that different scattering angles, and different elements of the scattering phase matrix can hold information about particular microphysical properties. Therefore the development and use of scattering instrumentation (both in situ and remote) may contribute a plethora of useful information to supplement data gathered from 2D imaging probes. Of interest here is the linear depolarisation ratio which is typically measured at near back-scattering angles to determine particle sphericity (and thus discriminate between ice and liquid water). Further controlled measurements are therefore useful in examining the sensitivity of linear depolarisation ratio on various microphysical characteristics, and also to test the ability of scattering models to recreate these results. In the work presented here, the linear depolarisation ratios were measured experimentally for a variety of ice crystal habits at scattering angles of 178°, 179° and 180° at temperatures between −7 °C and −30 °C. Measured depolarisation ratios are presented for several habits including solid and hollow columns, plates, sectored plates and dendrites. These results are compared with modelled results from Ray Tracing [40], and the applicability of this scattering model is discussed.

2. Methods

2.1. Experimental methods

2.1.1. Production of the cloud

This work was conducted in the Manchester Ice Cloud Chamber (MICC) as described in previous papers [32,10]. The cloud chamber is a 10 m tall by 1 m diameter cylindrical fall tube which is housed over three floors, in three stacked cold rooms. The chamber can maintain temperatures down to −50 °C, and the temperature is monitored via 10 equidistant thermocouples which are placed along the length of the chamber.

For this particular experiment, the chamber is humidified using a water boiler, which introduces water vapour near the centre of the chamber as shown in Fig. 1. After the chamber has been humidified, the boiler is switched off; ice is then nucleated at the top of the chamber using the 'air popper' technique [32,10,41]. The air popper utilises a

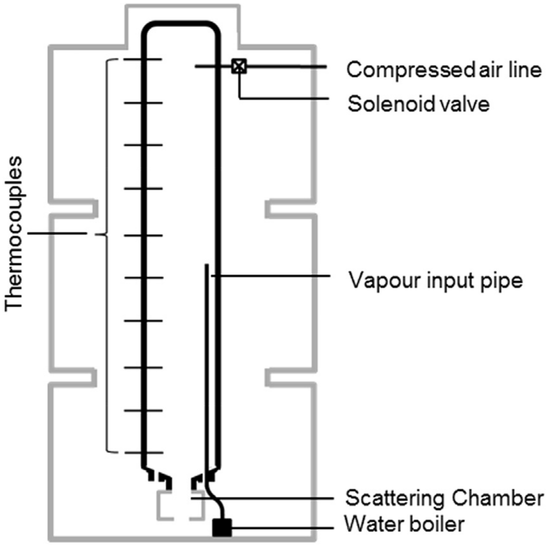

Fig. 1. The Manchester Ice Cloud Chamber (MICC) and set-up for experiments.

solenoid valve connected to a compressed air line. When the valve is opened, the air expands adiabatically, causing localised cooling down to about $-80\,^{\circ}\mathrm{C}$ [10], therefore causing the nucleation of ice. These nuclei fall through the chamber, growing at the expense of the water vapour, before falling out of the sampling port at the bottom. The particles then fall into a scattering chamber, where the optical measurements are taken. As time increases, the vapour in the chamber is depleted, causing a drop in humidity, and we see a change in particle habit with respect to time. Due to the vertical inhomogeneity of this set-up, representative values of humidity could not be taken, and therefore emphasis is given to particle habit, rather than the environmental conditions responsible for their formation. For each experiment, the temperature is kept constant.

2.1.2. Classification of particle habit

To determine particle habit, formvar replicas were taken every 60 s throughout the course of the experiment. To do this, a 1% weight to volume solution of formvar in chloroform was made. The solution was applied to microscope slides on which crystals were collected from the base of the cloud chamber. Each slide typically captured hundreds of ice crystals, these were later photographed under an optical microscope. Using the microscope graticule, the lengths of the basal, b, and prism facets, p, were measured. Aspect ratio, α, and maximum dimension, D, were then calculated using:

$$\alpha = p/b \tag{1}$$

and

$$D = \sqrt{p^2 + b^2} \tag{2}$$

where

p	length of the prism facet
b	length of the basal facet
α	aspect ratio
D	maximum dimension

For plate-like particles, which tended to fall with basal facets parallel to the microscope slide, the lengths of the prism facets could not be measured with the microscope graticule. Instead, the microscope was focussed on the top and bottom facets of the crystals respectively, and the vernier scale on the microscope was used to estimate plate thickness.

2.1.3. Scattering chamber and optical set-up

Optical measurements were taken in the 'scattering chamber' which was placed at the bottom of the cloud chamber. The scattering chamber is a 0.8 m × 0.8 m × 0.4 m container, with a 0.3 m opening at the top which was attached to a cloud chamber sample port as shown in Fig. 1. A rotating platform was mounted at the bottom of the scattering chamber, on which the detector optics were mounted. A plan view of the set-up is given in Fig. 2. A fan was placed beneath the scattering chamber in order to encourage the randomisation of particle orientation.

The laser source used in these experiments was a Hercules 2000 532 nm diode laser from laserglow technologies. The laser was housed in a temperature and humidity controlled enclosure outside of the scattering chamber. The beam was firstly passed through a wire grid polariser, thus polarising the beam perpendicular to the scattering plane. The beam was then directed through a faraday isolator, which prevents back reflections from re-entering the laser. The beam then exited the laser enclosure and entered the scattering chamber, where it fell upon a 50:50 non-polarising pellicle beam splitter, mounted at 45° to the incident beam. The beam splitter directed the reflected beam through the cloud, while the transmitted beam was extinguished on a beam stop at the far side of the chamber. The reflected beam was scattered by cloud particles in the sample volume. The use of a non-polarising beam splitter allowed 50% of the light scattered at 180° to be transmitted back through the beam splitter without altering the polarisation, thus allowing the measurement of linear depolarisation ratio at exactly 180°. Measurements were also taken at 179° and 178°. The portion of directly back scattered light which was reflected by the beam splitter was diverted via the faraday isolator and therefore did not re-enter the laser. The detector head collected scattered light in a solid angle element of 0.035 sr. Inside the detector head, a Glan–Taylor polarisation cube separated the scattered light into s and p components. The two components were focussed down via two plano-convex lenses onto two fibre optic heads. The fibre optic cables were connected at the other end to two amplified Si photodetectors, which measured the intensity of the two components. The linear depolarisation ratio was found by taking the ratio of the perpendicular and parallel components of the scattered light, where parallel and

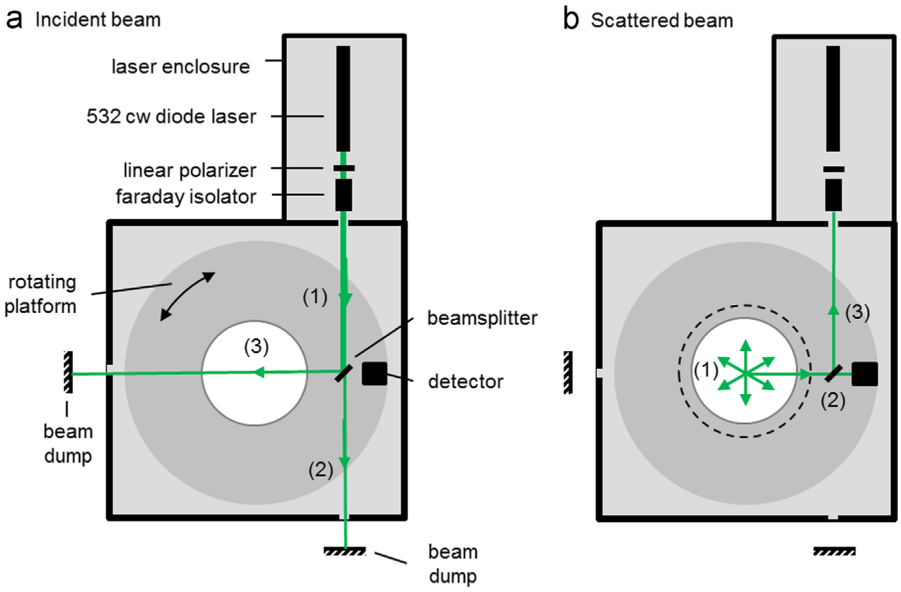

Fig. 2. (a) shows the set-up of the optical elements in the scattering chamber, and the path of the incident beam. The laser beam was passed through a polariser and an isolator (1), before falling incident on the beamsplitter. The transmitted beam (2) was extinguished, while the reflected beam (3) passed through the chamber, before it was also extinguished. (b) shows the path of the scattered beam: cloud particles fell through the area bounded by the dotted line, light was scattered in all directions (1), the directly backscattered portion fell incident on the beamsplitter (2), where the reflected portion (3) was diverted by the isolator, and the transmitted portion was measured by the detector. The detector was fixed to the rotating platform, allowing the measurement angle to be changed. The beamsplitter was attached to a fixed platform and therefore remains stationary.

perpendicular are defined relative to the incident beam:

$$\delta = \frac{I_{\perp} - I_{\perp(bg)}}{I_{\parallel} - I_{\parallel(bg)}} \tag{3}$$

where

δ	linear depolarisation ratio
$I_{\perp}$	intensity of the perpendicular component
$I_{\perp(bg)}$	background intensity of the perpendicular component
$I_{\parallel}$	intensity of the parallel component
$I_{\perp(bg)}$	background intensity of the parallel component

As various optical elements can be affected by environmental conditions, care was taken to mitigate the effects of temperature and humidity on the optical components. Where possible, equipment was housed in the laser enclosure (which was actively heated, and dried using desiccant), or in the case of the photodetectors, housed outside of the cold room entirely. The beam splitter and detector head were required to be mounted inside the scattering chamber, so low voltage heating elements were applied to the mounting posts, and small fans were used to create a local air flow over the optical surfaces. This approach was found to remove/prevent condensation which would have affected polarisation measurements.

2.2. Calibration of the photodetectors

Two broadband (320–1100 nm) Thorlabs Si Transimpedance Amplified Photodetectors were used to measure the parallel and perpendicular polarised components of the scattered beam. Each photodetector outputs a voltage (V), which is a function of the incident light power (P), wavelength responsivity (R), and gain (G), given by

$$V = P \cdot R(\lambda) \cdot G \tag{4}$$

These experiments use a single 532 nm radiation source, and therefore, knowledge of the full spectral responsivity, $R(\lambda)$, is not required. Instead, a combined responsivity-gain value, $G(\lambda = 532)$, was found for each of the two photodetector systems, including the effect of their collection optics. As the laser itself does not have a calibrated output, the gain was measured via a cross-calibration against an Ocean Optics S2000 CCD spectrometer system with direct input optics, which was calibrated independently against a NIST-traceable FEL 1 kW lamp. To find the gain for each photodetector system, the laser beam was split using a 50:50 pellicle beam splitter, and the reflected and transmitted beams were directed to the calibrated Ocean Optics collection optics, and the photodetector collection optics, respectively. Both sets of collection optics were placed equidistant from the beamsplitter, and aligned with the input beam by using target centred alignment optics to match the back reflections with the incident beam. A faraday isolator was used to prevent back reflections from re-entering the laser. This procedure was repeated using various neutral density filters to verify that the gains determined were stable across the measurable intensity range. This was again repeated for the second photodetector system. The calibration set-up is shown in Fig. 3.

The combined responsivity-gain is given by

$$G(\lambda = 532\ \text{nm}) = \frac{I_m - I_{m(bg)}}{V - V_{(bg)}} \tag{5}$$

where

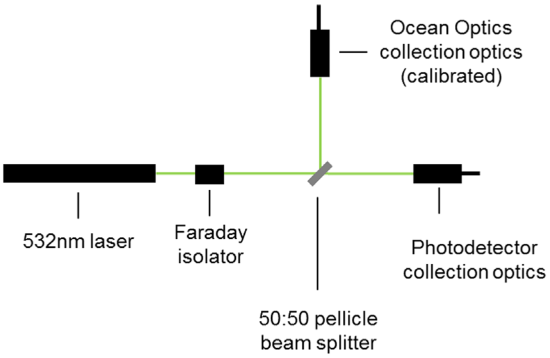

Fig. 3. The laser beam is directed onto a 50:50 pellicle beam splitter, aligned at 45° to the incident beam. The reflected 50% of the beam is directed onto the calibrated Ocean Optics CCD spectrometer collection optics, and the transmitted beam is directed onto the photodetector collection optics. The measured intensity from the calibrated instrument is used to find the gain of the non-calibrated photodetector system.

I_m	measured intensity from the CCD array spectrometer
$I_{m(bg)}$	measured background intensity from the CCD array spectrometer
V	photodetector output voltage
$V_{(bg)}$	photodetector background voltage

Any systematic errors in the Ocean Optics calibration and in the cross-calibration set-up will be removed by taking the ratio of the two photodetector channels to find the linear depolarisation ratio. In the experimental set-up, the two sets of photodetector collection optics were combined with a Glan–Taylor cube as described in Section 2.1.3. In this set-up, the measured gains for each detector were then confirmed by rotating the lasers' plane of polarisation and ensuring the expected ratios were produced.

2.3. Computational methods

Three particle models were used to describe typical geometries identified in the cloud chamber [32]. This includes the solid hexagonal prism, the hollow hexagonal prism with pyramidal indentations (henceforth referred to as the 'hollow 1' geometry), and hollow hexagonal prism with stepped hexagonal indentations (henceforth referred to as the 'hollow 2' geometry) as shown in Fig. 4.

The particles are constructed according to the maximum dimension, D, aspect ratio, α, cavity width, cw, and depth, cd, as shown in Fig. 5, where the cavity width and depth are defined as percentages of the prism and basal facets, respectively. By changing these variables, the particle models can cover a wide range of crystal morphologies as observed during the experiments. The particle models were used in a ray tracing code [40], with a wavelength of 532 nm and a complex refractive index of $1.3117 + (1.409 \times 10^{-9})i$ [42]. The ray tracing code outputs phase matrix elements, and therefore we must define the linear depolarisation ratio in terms of these. The intensity and polarisation of a beam can be described by its Stokes vector, (I, Q, U, V), where I gives the intensity and Q, U and V together describe the ellipticity, orientation and sense of the polarisation respectively. The Stokes vector for a beam scattered by a randomly oriented particle is related to the Stokes vector of the incident beam by [43]

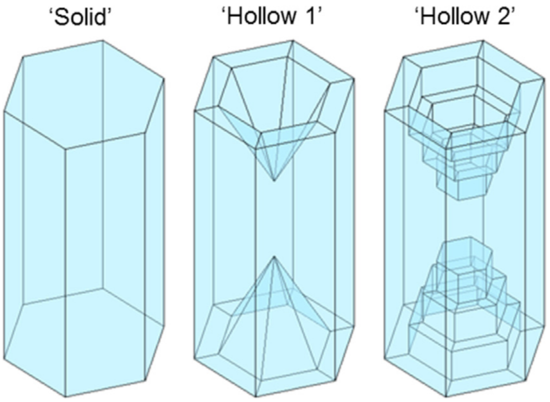

Fig. 4. From left to right: solid hexagonal model, hollow hexagonal model with pyramidal indentations ('hollow 1'), hollow hexagonal model with stepped indentations ('hollow 2'). Details of model construction can be found in Smith et al. [32].

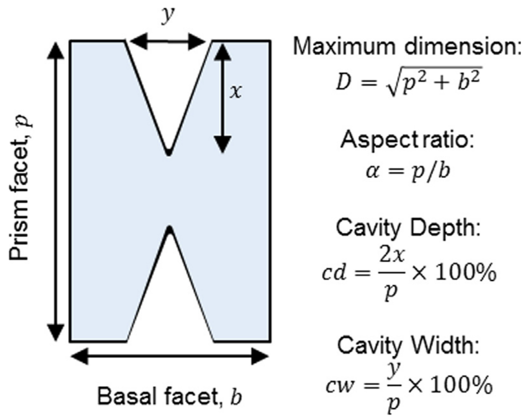

Fig. 5. Definitions of maximum dimension, aspect ratio, cavity depth and cavity with.

$$\begin{bmatrix} I_s \\ Q_s \\ U_s \\ V_s \end{bmatrix} = \frac{1}{k^2 r^2} \begin{bmatrix} P_{11} & P_{12} & 0 & 0 \\ P_{12} & P_{22} & 0 & 0 \\ 0 & 0 & P_{33} & P_{34} \\ 0 & 0 & -P_{34} & P_{44} \end{bmatrix} \cdot \begin{bmatrix} I_0 \\ Q_0 \\ U_0 \\ V_0 \end{bmatrix} \tag{6}$$

where

k	wavenumber
r	distance from the scatterer to the observer
P_{ij}	phase Matrix elements
$I_{0,s}$	incident and scattered intensities, respectively
$Q, U, V_{0,s}$	Stokes vectors describing polarisation for the incident and scattered beams, respectively.

In this experiment, the beam is linearly polarised in the y-plane, and therefore the incident Stokes vector can be given by

$$\begin{bmatrix} I_0 \\ Q_0 \\ U_0 \\ V_0 \end{bmatrix} = I_0 \begin{bmatrix} 1 \\ -1 \\ 0 \\ 0 \end{bmatrix} \tag{7}$$

Putting this into Eq. (6), gives

$$\begin{bmatrix} I_s \\ Q_s \\ U_s \\ V_s \end{bmatrix} = \frac{I_0}{k^2 r^2} \begin{bmatrix} P_{11} & P_{12} & 0 & 0 \\ P_{12} & P_{22} & 0 & 0 \\ 0 & 0 & P_{33} & P_{34} \\ 0 & 0 & -P_{34} & P_{44} \end{bmatrix} \cdot \begin{bmatrix} 1 \\ -1 \\ 0 \\ 0 \end{bmatrix} \tag{8}$$

giving

$$\begin{bmatrix} I_s \\ Q_s \\ U_s \\ V_s \end{bmatrix} = \frac{I_0}{k^2 r^2} \begin{bmatrix} P_{11}-P_{12} \\ P_{12}-P_{22} \\ 0 \\ 0 \end{bmatrix} \tag{9}$$

So the Stokes vectors of the scattered light can be given by

$$I_s = \frac{I_0}{k^2 r^2}(P_{11}-P_{12}) \tag{10}$$

$$Q_s = \frac{I_0}{k^2 r^2}(P_{12}-P_{22}) \tag{11}$$

$$U_s = 0 \tag{12}$$

$$V_s = 0 \tag{13}$$

The intensities in the x and y planes are given by

$$I_x = \tfrac{1}{2}(I_s + Q_s) \tag{14}$$

$$I_y = \tfrac{1}{2}(I_s - Q_s) \tag{15}$$

As the incident beam is polarised in the y plane, the linear depolarisation ratio is given as

$$\delta = \frac{I_x}{I_y} = \frac{I_s + Q_s}{I_s - Q_s} \tag{16}$$

In terms of the phase matrix elements, this can be expressed as:

$$\delta = \frac{P_{11} - P_{22}}{P_{11} - 2P_{12} + P_{22}} \tag{17}$$

We make use of Eq. (17) to find the linear depolarisation ratio from the ray tracing simulations of P_{11}, P_{12} and P_{22}. The ray tracing model cannot simulate direct forward or backscattering and has minimum and maximum scattering angles of 0.25° and 179.75° respectively. Therefore we cannot directly compare the exact backscattering measurements with modelled results.

3. Results

3.1. Experimental results

Experiments were conducted at three temperatures: −7 °C, −15 °C and −30 °C. In each experiment, particle habit in the scattering volume was found to change with respect to time due to the drop in humidity in the cloud chamber. As discussed in Section 2, reliable humidity measurements could not be taken in this and therefore emphasis is given to particle habit rather than humidity. Formvar replicas were taken every minute throughout the course of each experiment, yielding several hundred replicas per experiment. The replicas were then examined under a microscope to measure the maximum dimension, aspect ratio, cavity type, cavity depth and cavity width. These values were then used to create particle models for use in the ray tracing code, so that measured and modelled results could be compared. Details of the model constructions can be found in [32]. Each data point presented for modelled data represents results from *one* particle geometry. That is, the average particle geometry as observed from microscope measurements at a particular point in time for each experiment (as defined in Figs. 7, 10 and 13).

3.1.1. Experiments at −7 °C

Photographs of the formvar replicas from −7 °C experiments are shown in Fig. 6. We see that the initial crystals grown during these experiments had large indentations, which appear pyramidal in shape. Crystals grown later in the experiment became less hollow, with cavity depth reducing, and cavity structure becoming slightly more complex. Eventually, ice crystals grown at the end of the experiment were entirely solid. Averaged structures based on microscope observations are given in Fig. 7. These numeric values were used to construct particle models, which were used in ray tracing. The linear depolarisation ratio was measured at 178°, 179° and 180°, and it was modelled at 178°, 179° and 179.75°. Measured and modelled results are shown in Fig. 8.

3.1.2. Experiments at −15 °C

Photographs of the formvar replicas from the −15 °C experiments are shown in Fig. 9. Similar to the −7 °C experiments, we see that the crystal habits become more pristine with time. Initial crystal samples show some dendritic features, whereas later crystals are simpler sectored plates. Crystals grown at the end of the experiment are simple solid plates. Again, several hundreds of crystal replicas were measured, these data are summarised in Fig. 10. Measured and modelled linear depolarisation ratios are given in Fig. 11.

3.1.3. Experiments at −30 °C

Photographs of the formvar replicas from the −30 °C experiments are shown in Fig. 12. Unlike the previous two experiments, all crystals imaged during this experiment have similar internal structures, with barely any solid crystals being imaged. During the first minute of the experiment, the cloud consisted only of droplets, but after two minutes the cloud became entirely glaciated. Initial crystal samples show hollow crystals with stepped cavities. Later samples also show similar cavities, however there is a noticeable change in the aspect ratio. A summary of crystal measurements is given in Fig. 13, and measured

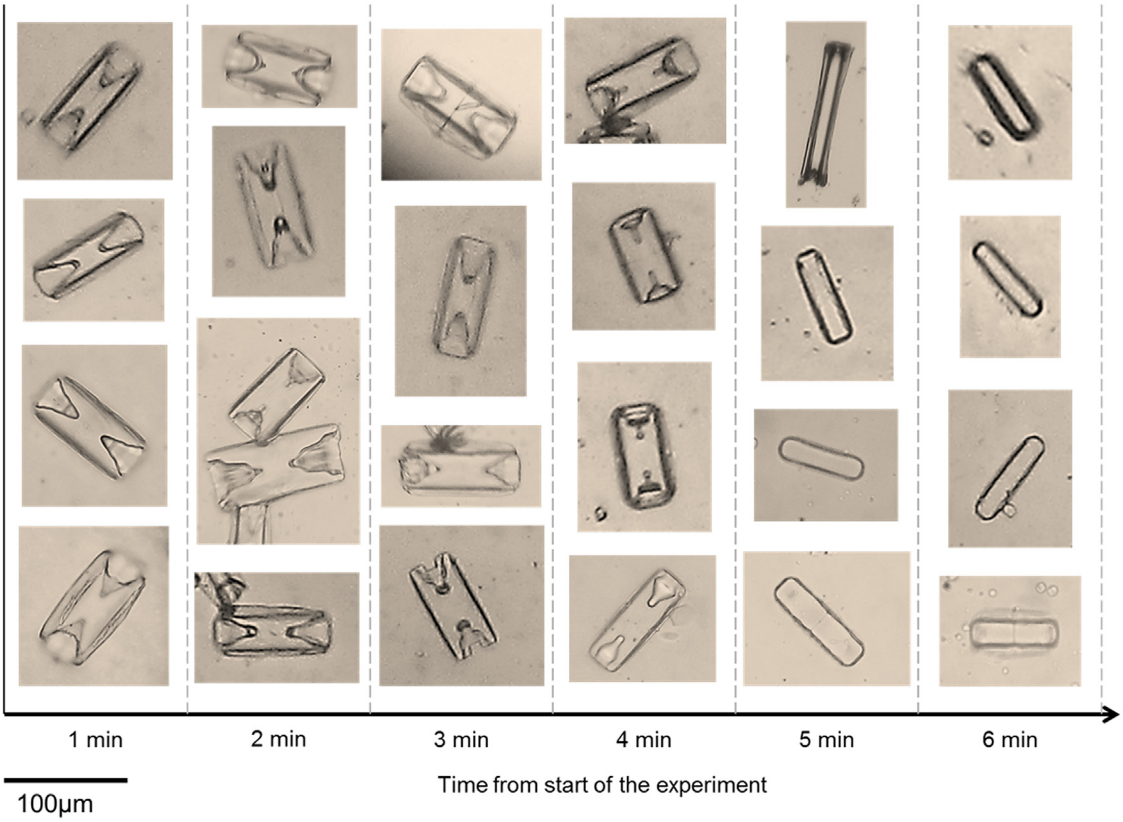

Fig. 6. Photographic images of formvar replicas collected during experiments conducted at −7 °C, plotted against time from nucleation.

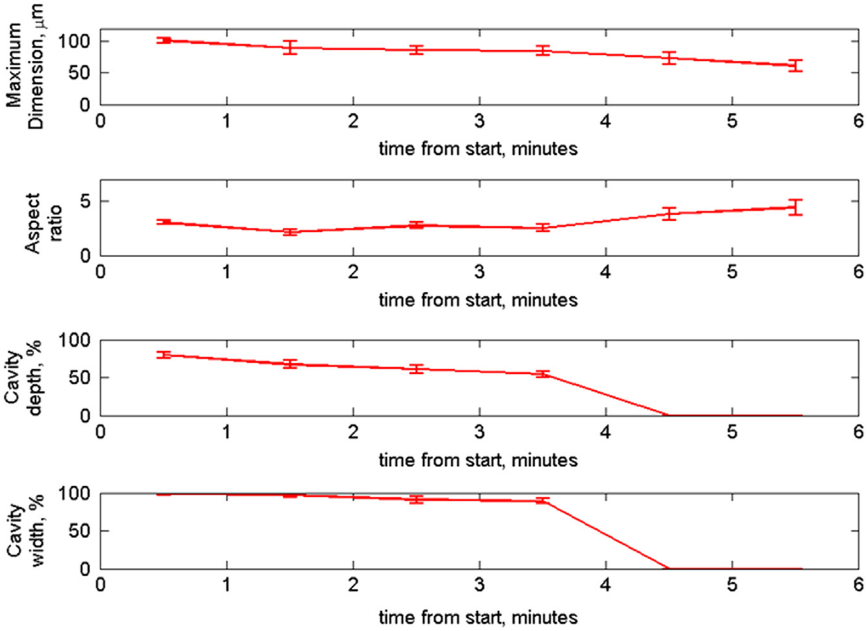

Fig. 7. Mean measured maximum dimension, aspect ratio, cavity depth and cavity width for replicas collected during experiments at −7 °C, plotted with respect to time.

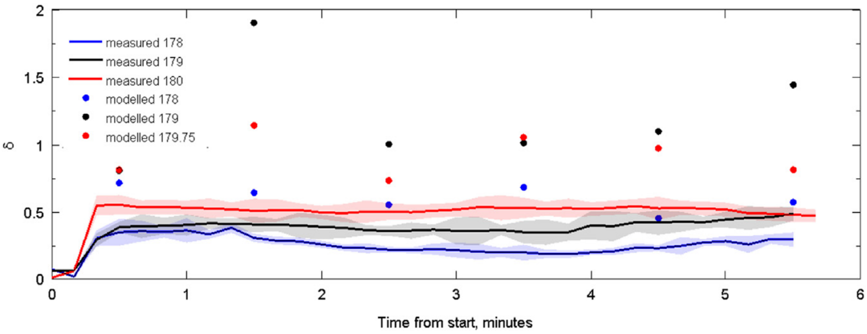

Fig. 8. Measured and modelled linear depolarisation ratios of solid and hollow columns produced at −7 °C. Standard deviations of measured results are shown as shaded regions.

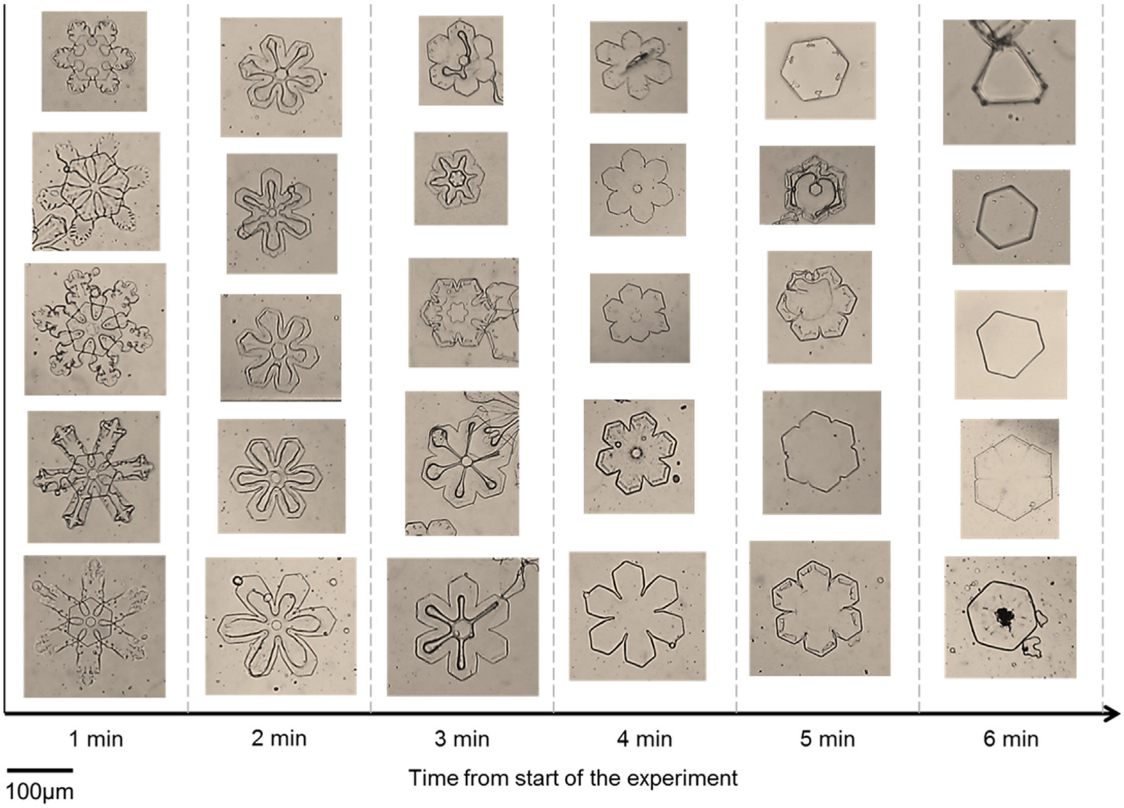

Fig. 9. Photographic images of formvar replicas collected during the −15 °C experiments, plotted against time from nucleation.

and modelled linear depolarisation ratios are given in Fig. 14.

3.2. Computational results

Several variables have already been highlighted as factors in the linear depolarisation ratio of ice crystals, including: aspect ratio, indentations (cavities), and surface roughness. Such variables are intrinsically linked and can therefore not be isolated in real experiments. Therefore, the individual effects of aspect ratio, cavity depth, cavity width and distortion are investigated theoretically.

3.2.1. Effect of aspect ratio on linear depolarisation ratio

Linear depolarisation ratio was calculated for three types of crystal geometry: solid hexagonal prisms, hollow hexagonal prisms with pyramidal cavities, and hollow hexagonal prisms with hexagonal cavities. The maximum dimension was set to a constant of 100 μm, the cavity depth and width were set to 50% and 80%, respectively, and the aspect ratio was varied. The left hand plot in Fig. 15 shows the near backscattering simulations of the three crystal geometries with respect to aspect ratio. We see in general that the hollow 2 particles are less sensitive to changes in aspect ratio, whereas both the solid prisms and the hollow 1 particles show a greater range in

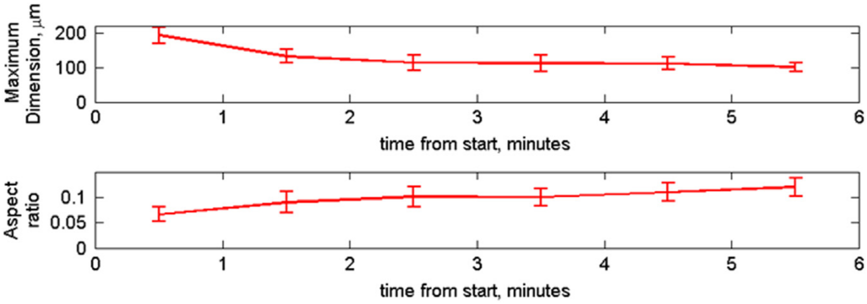

Fig. 10. Mean measured maximum dimension, aspect ratio, cavity depth and cavity width for the −15 °C experiments, plotted with respect to time.

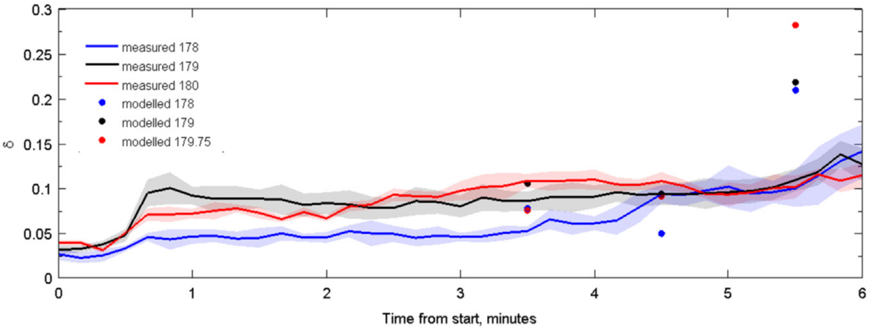

Fig. 11. Measured and modelled linear depolarisation ratios of dendrites/sectored plates/plates. Standard deviations of measured results are shown as shaded regions.

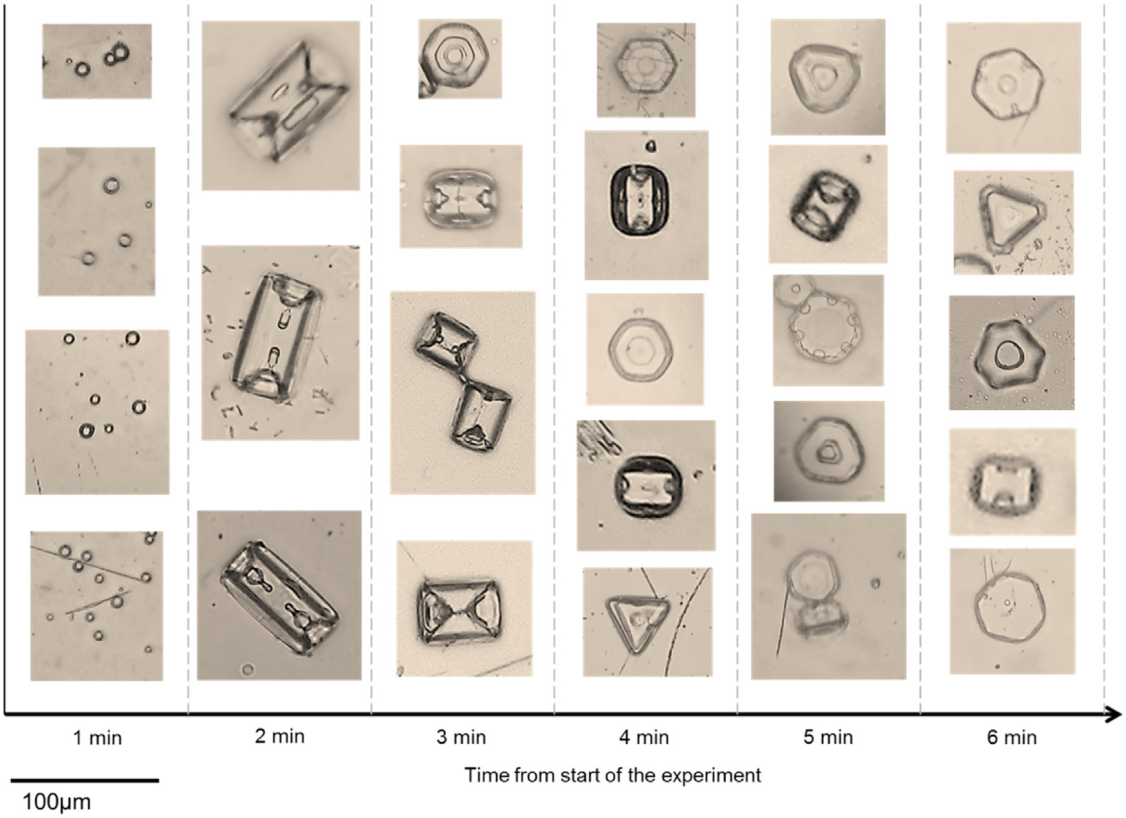

Fig. 12. Photographic images of formvar replicas collected during the −30 °C experiments, plotted against time from nucleation.

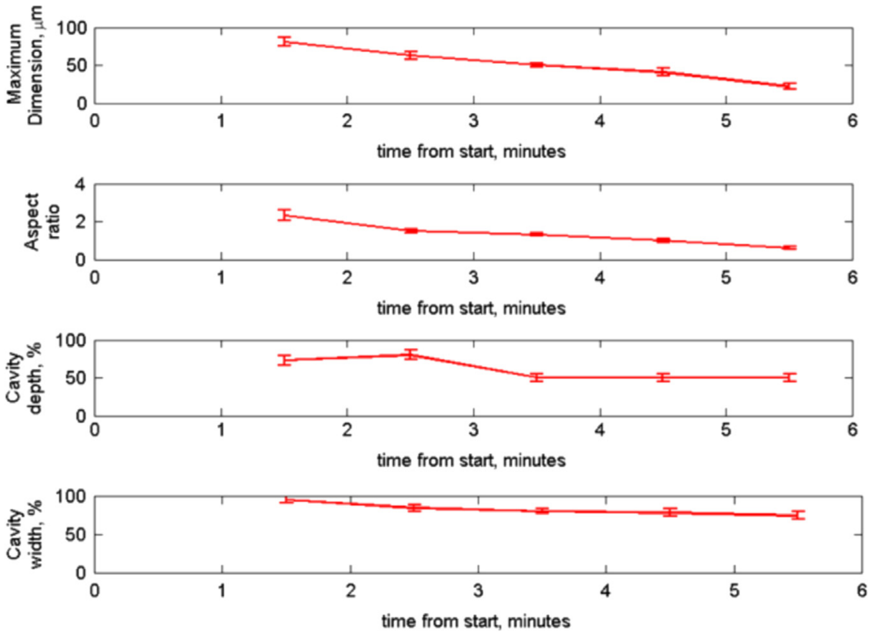

Fig. 13. Mean measured maximum dimension, aspect ratio, cavity depth and cavity width for the −30 °C experiments, plotted with respect to time.

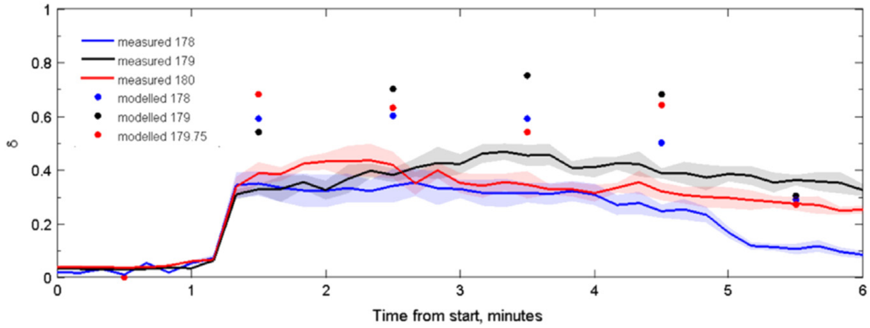

Fig. 14. Measured linear depolarisation ratios at 178°, 179° and 180° (solid line), and modelled values from ray tracing. Standard deviations of measured results are shown as shaded regions.

depolarisation at near backscattering angles. Although this paper focuses on the backscattering linear depolarisation ratio, the ray tracing code outputs phase matrix elements for the angular range 0.25–179.75°, therefore the linear depolarisation ratio over the full angular range is discussed. The right hand plot in Fig. 15 shows the linear depolarisation ratios over all angles for all three crystal geometries with varying aspect ratio. We see that the hollow 1 particle shows the greatest variation in linear depolarisation ratio at forward scattering angles where it appears to be very sensitive to aspect ratio.

3.2.2. Effect of cavity depth on linear depolarisation ratio

In this paper, we present two geometries for the internal structure of hollow ice crystals. The ‘hollowness’ is defined as the length of both cavities expressed as a percentage of the length of the prism facet. To investigate the effect of cavity depth on the linear depolarisation ratio, Ray Tracing results were computed for particles of varying degrees of hollowness, from 0% to 97.5%. Since it is evident that linear depolarisation ratio is sensitive to aspect ratio, particularly for aspect ratios less than 1, these calculations were repeated for particles of aspect ratios of 0.2, 0.4, 0.8 and 1.6. For these calculations the maximum dimension was fixed at 100 μm, and the cavity width was fixed at 80%. Fig. 16 shows the modelled, near backscattering linear depolarisation ratios for the two hollow particles with varying cavity depths.

From Fig. 16, we see that for the hollow 1 particle (pyramidal cavities), there is no obvious correlation between cavity depth and linear depolarisation ratio. By comparison, for the hollow 2 particle, we see a general decrease in linear depolarisation ratio with respect to cavity depth at scattering angles of 178° and 179°. However, at 179.75°, the linear depolarisation seems insensitive to cavity depth. Fig. 17 shows the modelled linear depolarisation ratios for the full range of scattering angles calculated (0.25–179.75°).

From Fig. 17 we see that the 0–20° region is particularly sensitive to the presence of pyramidal indentations, with

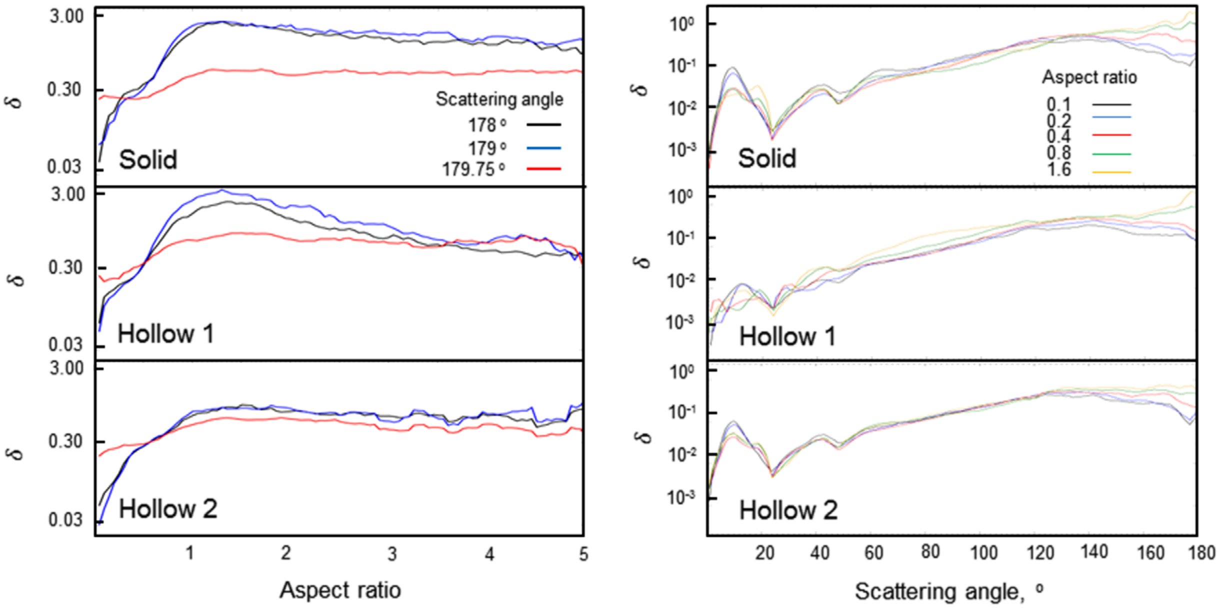

Fig. 15. Left: linear depolarisation ratios at near backscattering angles (178°, 179° and 179.75°) for solid (top), hollow 1 (middle) and hollow 2 (bottom) crystals at varying aspect ratios. Right: linear depolarisation ratios between 0.25° and 179.75° for solid (top), hollow 1 (middle) and hollow 2 (bottom) crystals at aspect ratios of 0.1, 0.2, 0.4, 0.8 and 1.6.

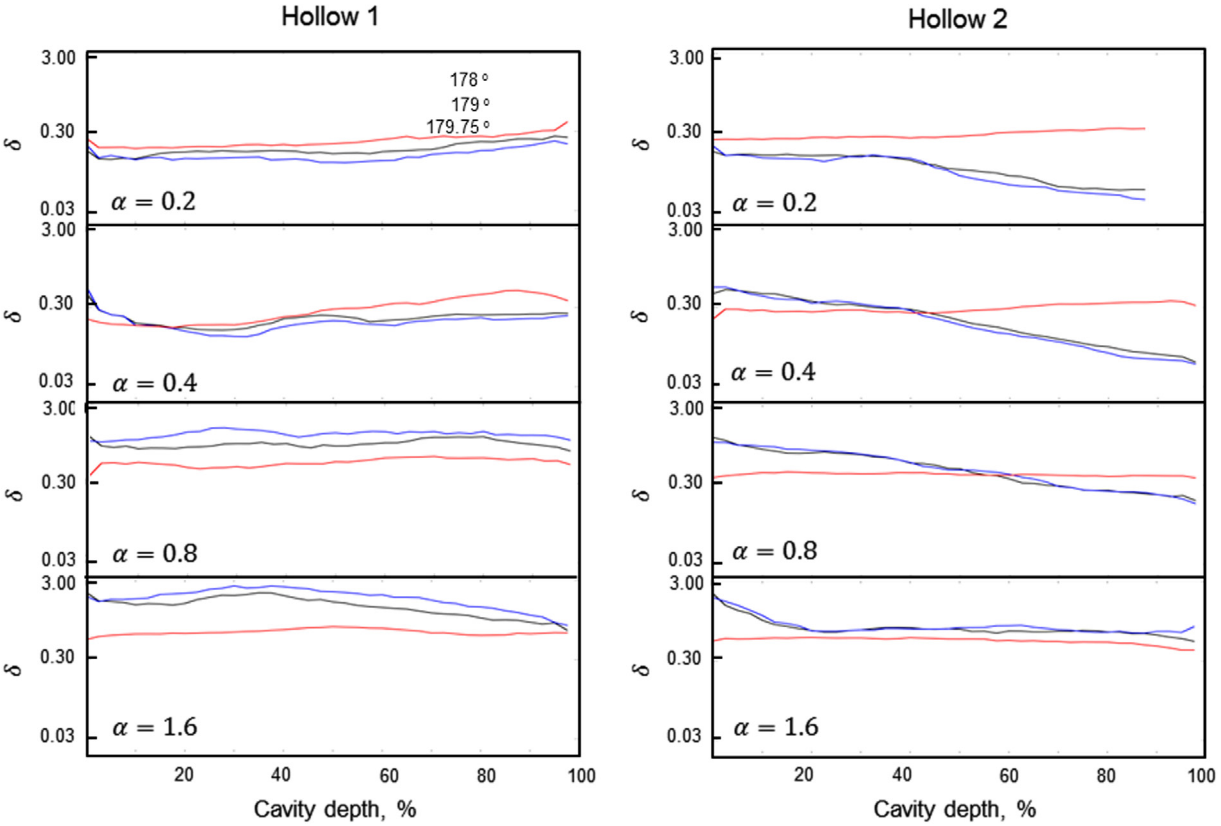

Fig. 16. Modelled near backscattering linear depolarisation ratios of two hollow cavity types with varying cavity depth and aspect ratio. The left hand side shows results from the hollow 1 particle (pyramidal cavities), whereas the right hand side shows results from the hollow 2 particle (stepped cavities).

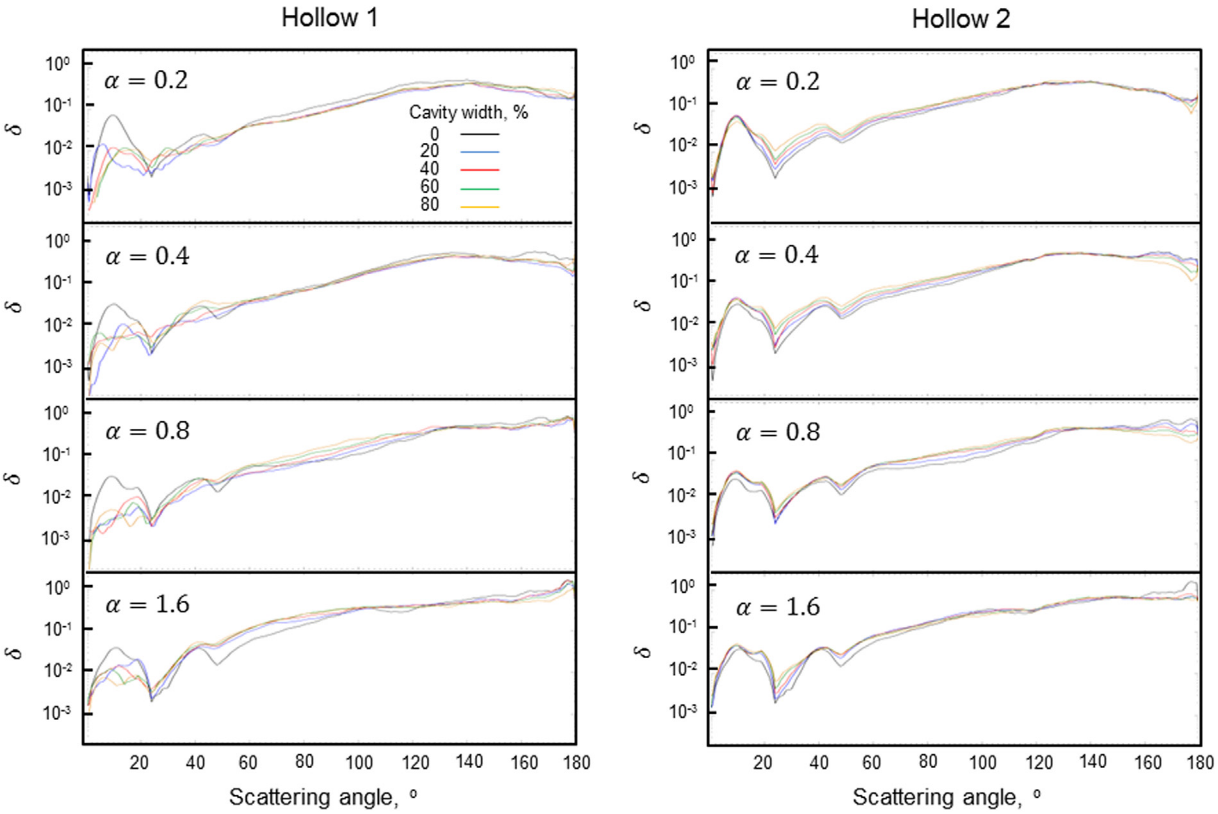

Fig. 17. Modelled linear depolarisation ratios for two types of hollow column with varying aspect ratio and cavity depth. The left column shows results from the hollow 1 geometry (pyramidal indentations), and the right column shows results from the hollow 2 geometry (stepped indentations). Different traces represent cavity depths of 0, 20, 40, 60 and 80%.

an evident drop in linear depolarisation ratio. However, the same effect is not observed for particles with stepped cavities. It can also be seen that, at larger scattering angles ($\geq 160°$), the linear depolarisation ratio is more sensitive to changes in the stepped cavity, when compared with the pyramidal cavity.

3.2.3. *Effect of cavity width on linear depolarisation ratio*

In addition to the cavity depth, simulations were also run for particles of varying cavity width. For these calculations, the maximum dimension was again set to 100 μm, the cavity depth was set to 50%, and the cavity width was varied in 5% increments from 0% to 95%. Simulations were run for aspect ratios of 0.2, 0.4, 0.8 and 1.6.

From Fig. 18, we see that there is little dependence on the cavity width for the linear depolarisation ratio of hollow 1 particles. On the other hand, hollow 2 particles show a general decrease in linear depolarisation ratio with respect to increasing cavity width. Similar to simulations investigating the cavity depth, we again see that the forward scattering region (0–50°) is affected by the cavity width of the hollow 1 particles, although the same effect is not observed for the hollow 2 particles.

3.2.4. *Effect of distortion on linear depolarisation ratio*

To approximate the effect of surface roughness, simulations were run with varying values of the distortion parameter, *s*. The distortion parameter approximates surface roughness by tilting the surface normal for an incoming ray. The tilt angle is defined by a random number up to a maximum, which is defined by the distortion parameter [40]. However, it has been shown that by using uniformly distributed tilt angles, the angular scattering intensities are poorly modelled. Therefore we use a modified code where the probability distribution function of the tilt angles is described by a Weibull distribution [44,45]. Similar to previous simulations, the maximum dimension was set to 100 μm, the cavity depth was set to 50%, and the cavity width was set to 80%. Simulations were run for aspect ratios of 0.2, 0.4, 0.8 and 1.6. Firstly we investigate the effects of distortion on the linear depolarisation ratios of solid columns, shown in Fig. 20.

From Fig. 20 (left), we see that for the weakly depolarising plate-like particles (α=0.2, 0.4), the use of distortion causes a general increasing trend in the linear depolarisation ratio for near backscattering angles. As the aspect ratio increases, and the prisms become more strongly depolarising (α=0.8, 1.6), we see a general decrease in linear depolarisation ratio for scattering angles 178° and 179° for small values of distortion. For aspect ratios of 0.8 and 1.6, the linear depolarisation ratios at scattering angles 178° and 179° reach a minimum at a distortion parameter of ≈ 0.12, before increasing again. These minima correspond to maximum decreases in

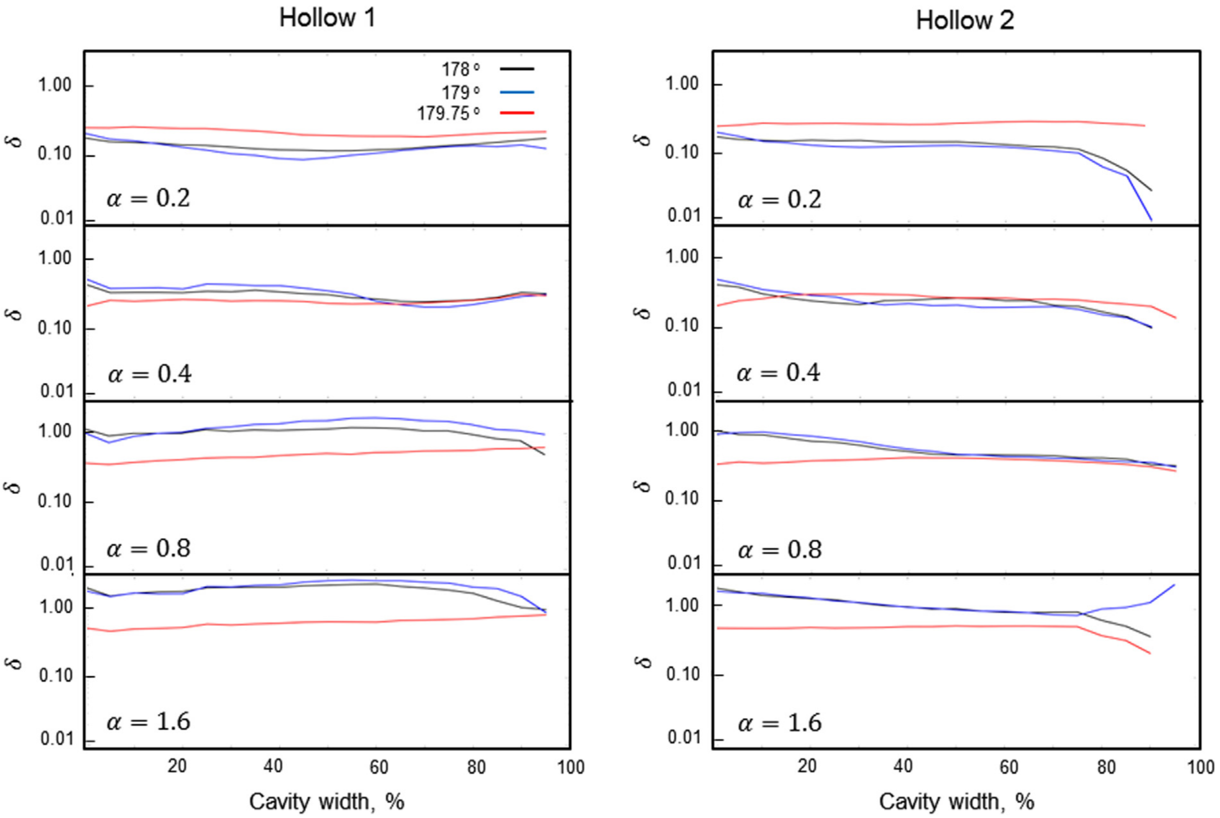

Fig. 18. Modelled near backscattering linear depolarisation ratios of two hollow cavity types with varying cavity width and aspect ratio. The left hand side shows results from the hollow 1 particle (pyramidal cavities), whereas the right hand side shows results from the hollow 2 particle (stepped cavities).

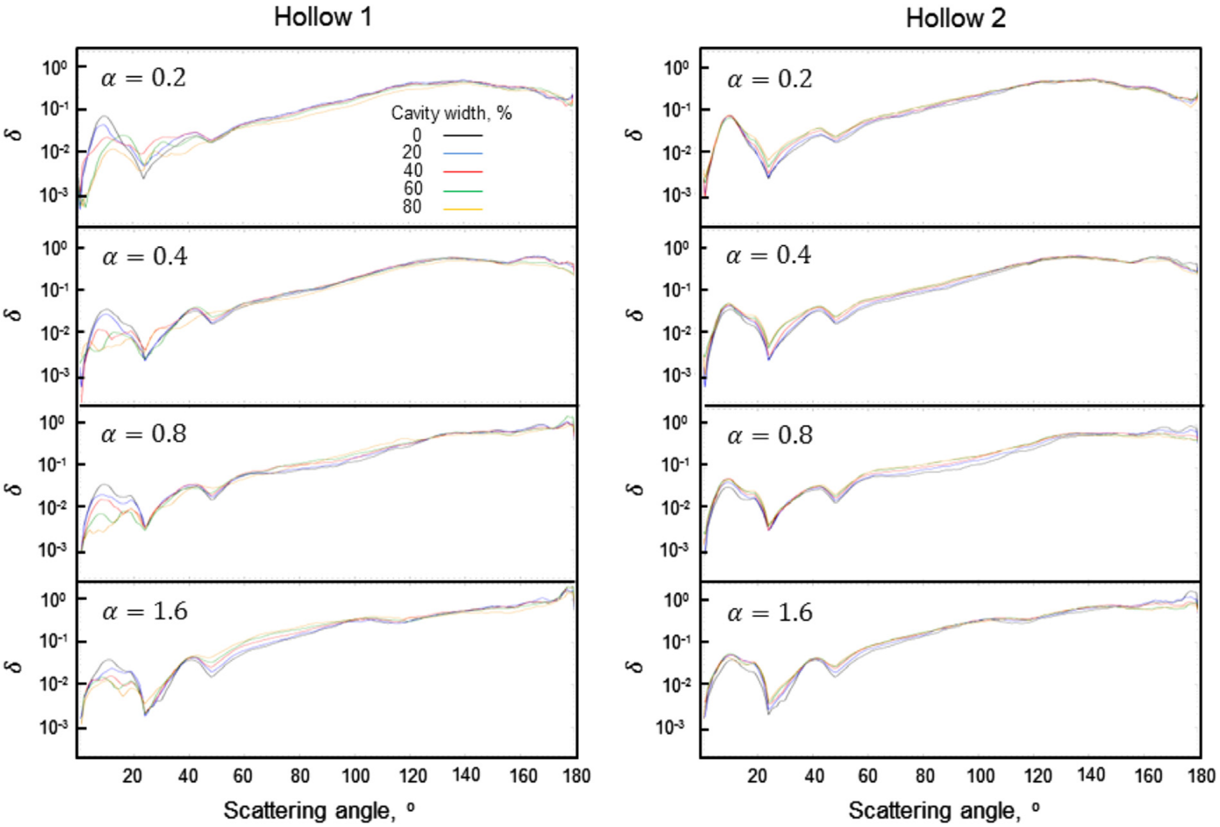

Fig. 19. Modelled linear depolarisation ratios for two types of hollow column with varying aspect ratio and cavity depth. The left column shows results from the hollow 1 geometry (pyramidal indentations), and the right column shows results from the hollow 2 geometry (stepped indentations). Different traces represent cavity widths of 0, 20, 40, 60 and 80%.

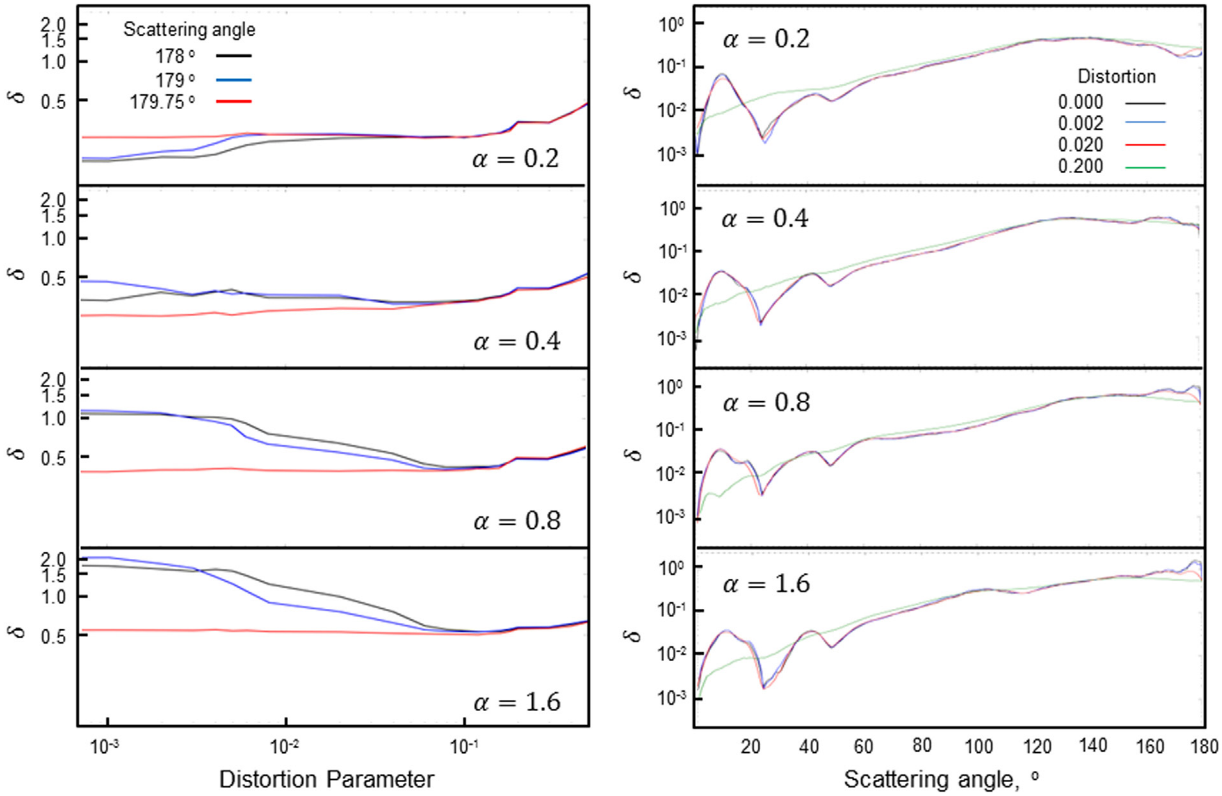

Fig. 20. Modelled linear depolarisation ratios for solid columns with varying values of distortion and aspect ratio. The left column shows near backscattering linear depolarisation ratios (178°, 179° and 179.75°) with varying distortion. The right columns show linear depolarisation ratios in the angular range 0.25–179.75° for solid columns with distortion parameters of 0, 0.002, 0.02 and 0.2.

predicted linear depolarisation ratio at near-backscattering angles of 61% and 73% for aspect ratios of 0.8 and 1.6 respectively (compared with simulations with zero distortion).

The same calculations were done for hollow 1 type columns, presented in Fig. 21. From this we see similar results to those obtained using solid columns (Fig. 20). Again, the weakly depolarising particles (α=0.2, 0.4) show a general increasing trend in linear depolarisation with the use of distortion. For the more strongly depolarising particles (α=0.8, 1.6), we again see an initial decrease in the linear depolarisation ratio, reaching minimum values at a distortion parameter of ≈ 0.14. These minimum values correspond to maximum decreases in predicted linear depolarisation ratio of 60% and 71% for aspect ratios of 0.8 and 1.6 respectively (for near backscattering angles).

Fig. 22 show the ray tracing calculations for hollow 2 type columns with varying degrees of distortion. Similar to both the solid columns and hollow 1 columns, plate like particles (α=0.2, 0.4) show a general increasing trend in linear depolarisation ratio with the use of distortion. For the more strongly depolarising particles (α=0.8, 1.6), the use of very small distortion values ($s < 0.005$) causes a initial increase in linear depolarisation ratio. Beyond this, increasing the distortion parameter causes a reduction in the linear depolarisation ratio, down to a minimum value at s=0.12, at which point the linear depolarisation begins to increase. These minimum values correspond to maximum decreases in predicted near-backscattering linear depolarisation ratios of 16% and 17% for aspect ratios 0.8 and 1.6 respectively. Therefore we see that the use of distortion on the hollow 2 column has a weaker impact on the linear depolarisation ratio when compared to solid or hollow 1 columns.

The right-hand columns of Figs. 20–22 shows the linear depolarisation ratios of the three crystal geometries with distortion values of 0, 0.002, 0.02 and 0.2 over the full angular range computed by the ray tracing code. For all three particle types, we see that the use of distortion has a significant effect on forward scattering regions with notable differences seen around the halo regions.

4. Conclusions

Measurements of the linear depolarisation ratio at exact and near backscattering angles were taken for various ice crystal habits. Results are presented here and compared with simulations from Ray Tracing. In general, it is found that modelled results from Ray Tracing over-predict the linear depolarisation ratio when compared to measured results. This is particularly true for the experiments conducted at −7 °C where particles had large aspect ratios, and were either solid, or contained pyramidal cavities. On average for this experiment, differences between measured and modelled results were ≈ 120%. Section 3.2.4 discusses

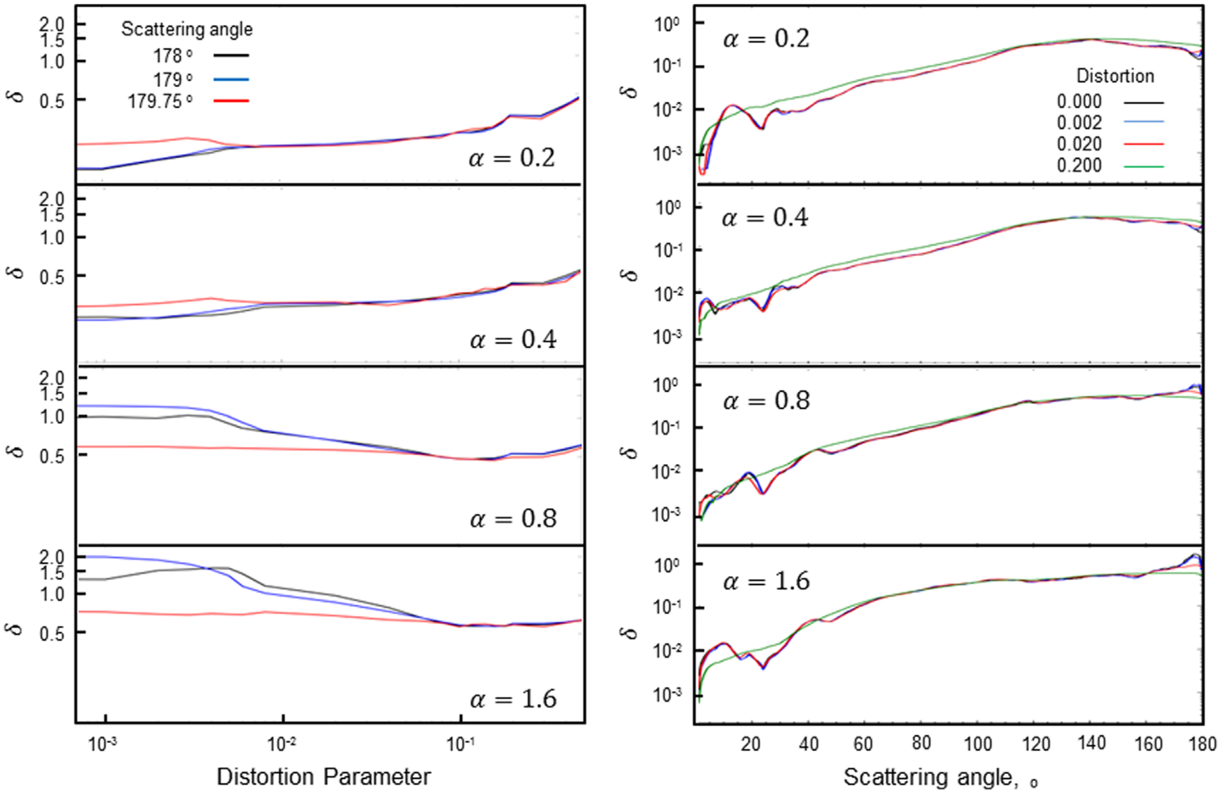

Fig. 21. Modelled linear depolarisation ratios for hollow 1 columns with varying values of distortion and aspect ratio. The left column shows near backscattering linear depolarisation ratios (178°, 179° and 179.75°) with varying distortion. The right columns show linear depolarisation ratios in the angular range 0.25–179.75° for hollow 1 columns with distortion parameters of 0, 0.002, 0.02 and 0.2.

the use of the distortion parameter to approximate surface roughness. For columnar particles, the use of the distortion parameter can lower the predicted linear depolarisation ratio which may explain, in part, the discrepancies between measured and modelled results.

At −15 °C, experimental and modelled results agree well for large plates and sectored plates observed between 3 and 5 minutes (9), however, for the smaller, pristine plates observed at the end of the experiments, modelled results largely over-predicted linear depolarisation ratio by up to 200%. Unlike the experiments conducted at −7 °C, the modelled results cannot be improved with the use of distortion. For plate like particles, the use of the distortion parameter causes an increase in the predicted linear depolarisation ratio (see Figs. 20–22). For such weakly depolarising particles, increasing the complexity of the particle by using distortion will cause linear depolarisation ratio to increase, due to the wave undergoing many more interactions. The discrepancy between measured and modelled results in this case may be due to the rounded particle edges as observed in Fig. 9, or other complexities not yet represented in the particle model.

For experiments conducted at −30 °C, all particles were found to have stepped internal structures, so these were modelled using the 'hollow 2' geometry. Again, modelled results over-predicted the linear depolarisation compared to measurements, but average differences were reduced to just 30%. In this experiment, particle habits transition from column-like to plate-like over time. Although distortion could be used to reduce the predicted linear depolarisation ratio of the initial columnar particles, it could not be applied to reduce the linear depolarisation ratio of plate-like particles observed towards the end. Similar to the −15 °C experiments, the discrepancy between measured and modelled results could be explained, in part, by the rounded edges of the particles, both external and internal.

It is known that there are limitations to the geometric optics approach and its applicability for the treatment of polarised scattering has been questioned [46]. This is important for those applying these techniques for the determination of cloud/aerosol properties. Indeed, results from this paper show large differences between measured and modelled results when assuming pristine solid hexagons, and hexagons with pyramidal cavities (Figs. 8 and 11). However, when the stepped hollow column is assumed, the predictions of linear depolarisation ratio become much more realistic (Fig. 14). Figs. 16 and 18 show a general decreasing trend in the linear depolarisation ratio with increasing cavity depth and cavity width, respectively. Although the particle models are based on measurements from crystal replicas, errors in the measurement of cavity depth and width may in part explain the discrepancy between measured and modelled results. This result serves to highlight the sensitivity of the scattering properties on small scale features. While limitations

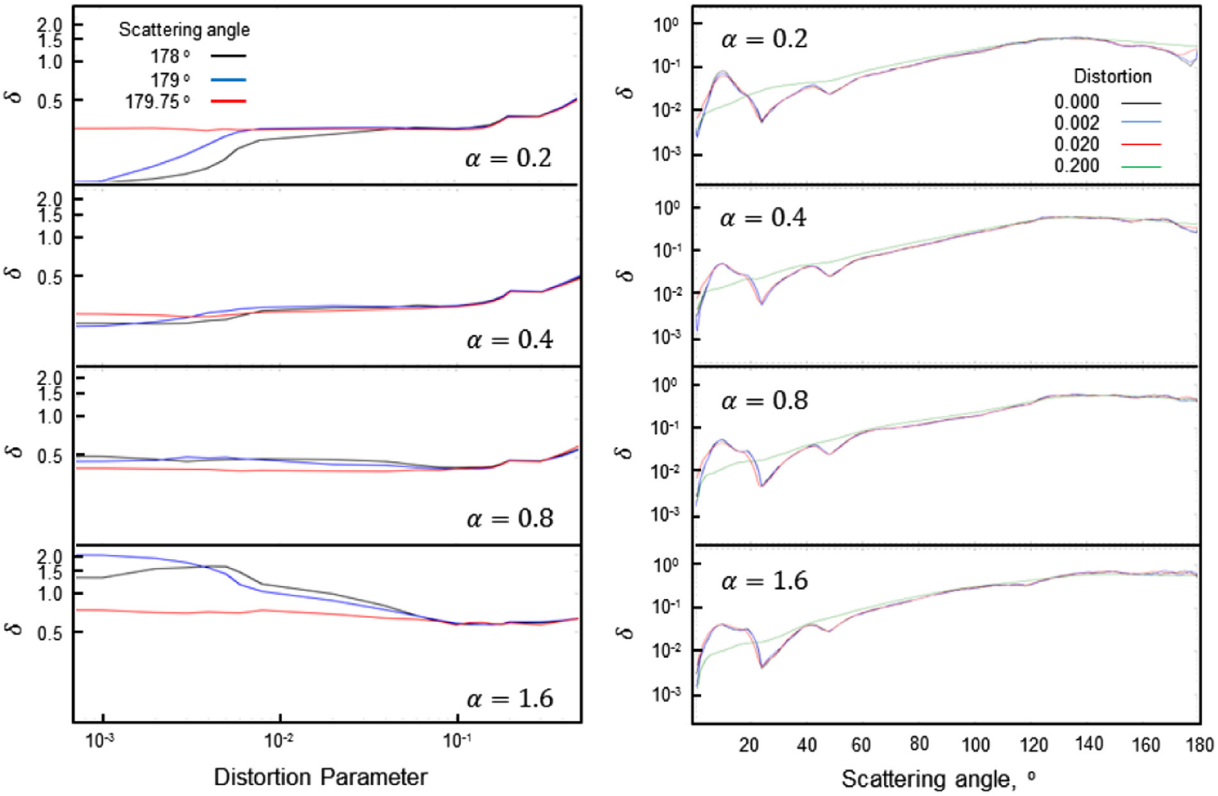

Fig. 22. Modelled linear depolarisation ratios for hollow 2 columns with varying values of distortion and aspect ratio. The left column shows near backscattering linear depolarisation ratios (178°, 179° and 179.75°) with varying distortion. The right columns show linear depolarisation ratios in the angular range 0.25–179.75° for hollow 2 columns with distortion parameters of 0, 0.002, 0.02 and 0.2.

of geometric optics are known, if more accurate scattering models are not applicable for larger and more complex crystal geometries, then geometric optics may be a suitable approximation when the particle geometries are better represented.

In addition to the backscattering region, ray tracing simulations show sensitivities to cavities at smaller scattering angles. In particular, the linear depolarisation ratio in the 0–20° region for a hollow 1 column is significantly lower than for a solid column. This difference is less significant for the hollow 2 column. For the hollow 1 column, the linear depolarisation ratio in the forward scattering region also shows sensitivity to the cavity depth and width as shown in Figs. 17 and 19. This sensitivity is not evident for the hollow 2 column, which appears more sensitive to changes in the cavity size at near backscattering angles as shown in Figs. 16 and 18. These dependencies may be used for the development of in situ instrumentation to measure linear depolarisation ratios at not only near backscattering angles, but at smaller angles too.

Although the results presented here focus on particle hollowness, other complexities are known to affect depolarisation, such as surface roughness, particle inclusions, and further deviations which have been observed are currently overlooked [35,36]. From the formvar images, we can clearly see that many of the particles exhibit rounded edges, this is particularly true for the indentations of the stepped hollow particles (12). This particle rounding is a likely contributor to the low values of linear depolarisation measured in these experiments. Further to the basal cavities presented here, indentations are often observed protruding from the prism facets, although their geometry is currently undetermined. There are also instances of scalene and trigonal particles in several of these experiments, which has also been noted in situ [47,48]. By incorporating these observed complexities, more physically representative particle models can be created and used to yield more reliable results from ray tracing calculations.

Acknowledgements

This work was funded by a Doctoral Training Grant (DTG) from the Natural Environment Research Council (NERC) in conjunction with a CASE award from Met Office UK. We would also like to acknowledge funding from the NERC ACID-PRUF program, Grant code NE/I020121/1, which supported experiments conducted in the Manchester Ice Cloud Chamber.

References

[1] IPCC. The physical science basis: contribution of working group 1 to the fifth assessment report of the IPCC. Cambridge University Press, Cambridge; 2013.

[2] Wendisch M, Pilewskie P, Pommier J, Howard S, Yang P, Heymsfield AJ, et al. Impact of cirrus crystal shape on solar spectral irradiance: a

case study for subtropical cirrus. J Geophys Res 110 (D3), 2005. http://dx.doi.org/10.1029/2004JD005294.

[3] Zhang Y, Macke A, Albers F. Effect of crystal size spectrum and crystal shape on stratiform cirrus radiative forcing. Atmos Res 1999;52:59–75.

[4] Baran AJ. A review of the light scattering properties of cirrus. J Quant Spectrosc Radiat Transfer 2009;110(14–16):1239–60. http://dx.doi.org/10.1016/j.jqsrt.2009.02.026.

[5] Lawson RP, Baker BA, Zmarzly P, O'Connor D, Mo Q, Gayet J-F, et al. Microphysical and optical properties of atmospheric ice crystals at south pole station. J Appl Meteorol Climatol 2006;45:1505–24.

[6] Lawson RP, O'Connor D, Zmarzly P, Weaver K, Baker B, Mo Q, et al. The 2D-S (stereo) probe: design and preliminary tests of a new airborne, high-speed, high-resolution particle imaging probe. J Atmos Ocean Technol 2006;23(1997):1462–77. http://dx.doi.org/10.1175/JTECH1927.1.

[7] Baumgardner D, Jonsson H, Dawson W, O'Connor D, Newton R. The cloud, aerosol and precipitation spectrometer: a new instrument for cloud investigations. Atmos Res 2001;59–60:251–64. http://dx.doi.org/10.1016/S0169-8095(01)00119-3.

[8] Grosvenor DP, Choularton TW, Lachlan-Cope T, Gallagher MW, Crosier J, Bower KN, et al. In-situ aircraft observations of ice concentrations within clouds over the Antarctic Peninsula and Larsen ice shelf. Atmos Chem Phys 2012;12(23):11275–94. http://dx.doi.org/10.5194/acp-12-11275-2012.

[9] Gallagher MW, Connolly PJ, Whiteway J, Figueras-Nieto D, Flynn M, Choularton TW, et al. An overview of the microphysical structure of cirrus clouds observed during EMERALD-1. Q J R Meteorol Soc 2005;131(607):1143–69. http://dx.doi.org/10.1256/qj.03.138.

[10] Connolly PJ, Emersic C, Field PR. A laboratory investigation into the aggregation efficiency of small ice crystals. Atmos Chem Phys 2012;12(4):2055–76. http://dx.doi.org/10.5194/acp-12-2055-2012.

[11] Jensen EJ, Lawson P, Baker B, Pilson B, Mo Q, Heymsfield AJ, et al. On the importance of small ice crystals in tropical anvil cirrus 2009: 5519–37. http://dx.doi.org/10.5194/acpd-9-5321-2009.

[12] Ramanathan V, Crutzen PJ, Kiehl JT, Rosenfeld D. Aerosols, climate, and the hydrological cycle. Science 2001;294:2119–24, http://dx.doi.org/10.1126/science.1064034.

[13] Loeb NG, Manalo-Smith N. Top-of-atmosphere direct radiative effect of aerosols over global oceans from merged CERES and MODIS observations. J Climate 2005;18:3506–26. http://dx.doi.org/10.1175/JCLI3504.1.

[14] Khain AP, Rosenfeld D, Pokrovsky A. Aerosol impact on the dynamics and microphysics of deep convective clouds. Q J R Meteorol Soc 2005;131:2639–63. http://dx.doi.org/10.1256/qj.04.62.

[15] Knollenberg RG. Techniques for probing cloud microstructure. In: Proceedings of the symposium on clouds—their formation, optical properties, and effects, May 13, 14, 1980, Williamsburg, VA (A82-12426 02-47). New York, Academic Press; 1981, p. 15–89 [Discussion, p. 90, 91, 1981, pp. 15–89].

[16] Dye JE, Baumgardner D. Evaluation of the forward scattering spectrometer probe. Part I: electronic and optical studies; 1984. http://dx.doi.org/10.1175/1520-0426(1984)001 < 0329:EOTFSS > 2.0.CO;2.

[17] Lance S, Brock CA, Rogers D, Gordon JA. Water droplet calibration of the Cloud Droplet Probe (CDP) and in-flight performance in liquid, ice and mixed-phase clouds during ARCPAC. Atmos Meas Tech 2010;3:1683–706. http://dx.doi.org/10.5194/amt-3-1683-2010.

[18] Ulanowski Z, Kaye PH, Hirst E, Greenaway R. Retrieving the size of particles with rough surfaces from 2D scattering patterns. AAPP 2011;89(1):1–5. http://dx.doi.org/10.1478/C1V89S1P084.

[19] Schnaiter M, Kaye PHP, Hirst E, Ulanowski Z, Wagner R. Exploring the surface roughness of small ice crystals by measuring high resolution angular scattering patterns. AAPP 2011;89(1): 5–8. http://dx.doi.org/10.1478/C1V89S1P084.

[20] Baumgardner D, Brenguier JL, Bucholtz a, Coe H, DeMott P, Garrett TJ, et al. Airborne instruments to measure atmospheric aerosol particles, clouds and radiation: a cook's tour of mature and emerging technology. Atmos Res 2011;102:10–29. http://dx.doi.org/10.1016/j.atmosres.2011.06.021.

[21] Baumgardner D, Newton R, Kramer M, Meyer J, Beyer A, Wendisch M, et al. The cloud particle spectrometer with polarization detection (CPSPD): a next generation open-path cloud probe for distinguishing liquid cloud droplets from ice crystals. Atmos Res 2014;142: 2–14. http://dx.doi.org/10.1016/j.atmosres.2013.12.010.

[22] Gerber H, Takano Y, Garrett TJ, Hobbs PV. Nephelometer measurements of the asymmetry parameter, volume extinction coefficient, and backscatter ratio in Arctic clouds. J Atmos Sci 2000;57:3021–34.

[23] Schnaiter M, Buttner S, Mohler O, Skrotzki J, Vragel M, Wagner R. Influence of particle size and shape on the backscattering linear depolarisation ratio of small ice crystals; cloud chamber measurements in the context of contrail and cirrus microphysics. Atmos Chem Phys 2012;12(21):10465–84. http://dx.doi.org/10.5194/acp-12-10465-2012.

[24] Sassen K, Liou KN. Scattering of polarized laser light by water droplet, mixed-phase and ice crystal clouds. part II: angular depolarizing and multiple-scattering behavior. J Atmos Sci 1979;36:852–61.

[25] Liou K-N, Lahore H. Laser sensing of cloud composition: a backscattered depolarization technique. J Appl Meteorol 1974;13: 257–63.

[26] Schotland RM, Sassen K, Stone R. Observations by lidar of linear depolarization ratios for hydrometeors. J Appl Meteorol 1971;10: 1011–7.

[27] Noel V, Winker D, McGill M, Lawson P. Classification of particle shapes from lidar depolarization ratio in convective ice clouds compared to in situ observations during crystalface. J Geophys Res: Atmos 109 (D24), 2004. http://dx.doi.org/10.1029/2004JD004883.

[28] Masuda K, Ishimoto H, Takashima T. Retrieval of cirrus optical thickness and ice-shape information using total and polarized reflectance from satellite measurements. J Quant Spectrosc Radiat Transfer 2002;75:39–51.

[29] Yang P, Hu YX, Winker DM, Zhao J, Hostetler Ca, Poole L, et al. Enhanced lidar backscattering by quasi-horizontally oriented ice crystal plates in cirrus clouds. J Quant Spectrosc Radiat Transfer 2003;79–80: 1139–57. http://dx.doi.org/10.1016/S0022-4073(02)00346-1.

[30] van Diedenhoven B, Cairns B, Fridlind AM, Ackerman AS, Garrett TJ. Remote sensing of ice crystal asymmetry parameter using multidirectional polarization measurements—Part 2: application to the research scanning polarimeter. Atmos Chem Phys 2013;13(6): 3185–203. http://dx.doi.org/10.5194/acp-13-3185-2013.

[31] Sassen K, Benson S. A midlatitude cirrus cloud climatology from the facility for atmospheric remote sensing. Part II: microphysical properties derived from lidar depolarization. J Atmos Sci 2001;58: 2103–12.

[32] Smith HR, Connolly P, Baran A, Hesse E, Smedley A, Webb A. Cloud chamber laboratory investigations into scattering properties of hollow ice particles. J Quant Spectrosc Radiat Transfer 2015;157: 106–18.

[33] Macke A, Mishchenko MI, Cairns B. The influence of inclusions on light scattering by large ice particles. J Geophys Res: Atmos 1996;101 (D18):23311–6. http://dx.doi.org/10.1029/96JD02364.

[34] Ulanowski Z, Hesse E, Kaye P, Baran A. Light scattering by complex ice-analogue crystals. J Quant Spectrosc Radiat Transfer 2006;100: 382–92.

[35] Baran AJ, Labonnote LC. On the reflection and polarisation properties of ice cloud. J Quant Spectrosc Radiat Transfer 2006;100: 41–54. http://dx.doi.org/10.1016/j.jqsrt.2005.11.062.

[36] Nousiainen T, Muinonen K. Surface-roughness effects on single-scattering properties of wavelength-scale particles. J Quant Spectrosc Radiat Transfer 2007;106(1–3):389–97. http://dx.doi.org/10.1016/j.jqsrt.2007.01.024.

[37] Takano Y, Liou K. Radiative-transfer in cirrus clouds. 3. Light-scattering by irregular ice crystals. J Atmos Sci 1995;52:818–37.

[38] Yang P, Zhang Z, Kattawar GW, Warren SG, Baum Ba, Huang H-L, et al. Effect of cavities on the optical properties of bullet rosettes: implications for active and passive remote sensing of ice cloud properties. J Appl Meteorol Climatol 2008;47(9):2311–30. http://dx.doi.org/10.1175/2008JAMC1905.1.

[39] Schnaiter M, Schon R, Mohler O, Saathoff H, Wagner R. Backscattering linear depolarization ratio of laboratory generated ice clouds composed of pristine and complex-shaped ice crystals. In: Tenth international conference on light scattering by non-spherical particles; 2007.

[40] Macke A, Mueller J, Raschke E. Single scattering properties of atmospheric ice crystals. J Atmos Sci 1996;53:2813–25.

[41] Rimmer J, Saunders C. Radiative scattering by artificially produced clouds of hexagonal plate ice crystals. Atmos Res 1997;45(2): 153–64. http://dx.doi.org/10.1016/S0169-8095(97)00022-7.

[42] Warren SG, Brandt RE. Optical constants of ice from the ultraviolet to the microwave: a revised compilation. J Geophys Res 2008;113 (D14):1–10. http://dx.doi.org/10.1029/2007JD009744.

[43] Van de Hulst HC. Light scattering by small particles. New York: John Wiley & Sons, Ltd; 1957.

[44] Shcherbakov V, Gayet J-F, Jourdan O, Ström J, Minikin A. Light scattering by single ice crystals of cirrus clouds. Geophys Res Lett 2006;33(15):L15809. http://dx.doi.org/10.1029/2006GL026055.

[45] Shcherbakov V, Gayet J-F, Baker B, Lawson P. Light scattering by single natural ice crystals. J Atmos Sci 2006;63:1513–25, http://dx.doi.org/10.1175/JAS3690.1.

[46] Yang P, Liou KN. Geometric-optics-integral-equation method for light scattering by nonspherical ice crystals. Appl Opt 1996;35(33):10–4.

[47] Murray BJ, Salzmann CG, Heymsfield AJ, Dobbie S, Neely RR, Cox CJ. Trigonal ice crystals in Earth's atmosphere. Bull Am Meteorol Soc 2015;96:1519–31. http://dx.doi.org/10.1175/BAMS-D-13-0012.

[48] Weickmann H. Die eisphase in der atmosphare. Ministry of Supply; 1948.